J. Fluid Mech. (2020), *vol.* 898, A4. © The Author(s), 2020.
Published by Cambridge University Press
doi:10.1017/jfm.2020.419

Péclet-number dependence of small-scale anisotropy of passive scalar fluctuations under a uniform mean gradient in isotropic turbulence

Tatsuya Yasuda[1,†], Toshiyuki Gotoh[1], Takeshi Watanabe[1] and Izumi Saito[1]

[1]Department of Physical Science and Engineering, Nagoya Institute of Technology, Gokiso-cho, Showa-ku, Nagoya, Aichi 466-8555, Japan

(Received 24 December 2019; revised 30 March 2020; accepted 20 May 2020)

We study passive scalar fluctuations convected by statistically stationary homogeneous isotropic turbulence under a uniform mean scalar gradient. In order to elucidate the parameter dependence of small-scale statistics of scalar fluctuations, we conduct direct numerical simulations of passive scalar turbulence with 59 different combinations of Reynolds number and Schmidt number. For all the cases, we compute time-average statistics of various quantities, which include the scalar derivative skewness and flatness, the ratio of parallel-to-perpendicular scalar-gradient variances, and the anisotropy parameter recently proposed (Hill, *Phys. Rev. Fluids*, vol. 2, 2017, 094601). Notably, the degree of small-scale anisotropy of passive scalar fluctuation is characterised by a universal function of the Péclet number $Pe_{\lambda_\theta} = u'\lambda_\theta/\kappa$, where u' is the root mean square velocity, λ_θ the Taylor microscale of scalar fluctuation, κ the mass diffusivity. In the definition of the Péclet number, the use of λ_θ, rather than the Taylor microscale of velocity fluctuation, is key to collapsing the data of different Reynolds and Schmidt numbers. When the Péclet number is low, large-scale anisotropic scalar structures emerge irrespective of the Reynolds number. These structures are elongated along the direction of the uniform mean scalar gradient, and their size is significantly larger than the integral length scale of velocity fluctuation.

Key words: turbulence theory, turbulent mixing, turbulence simulation

1. Introduction

Turbulent heat and mass transport processes are important in various engineering situations. For example, heat transport problems are concerned with heat exchangers, whereas mass transport phenomena are found in air pollutant dispersion. In general situations, a turbulent velocity field generates fluctuations in a scalar field via turbulent convection, and the fluctuating scalar field conversely affects the velocity field by local forces due to changes in temperature or mass concentration. Assuming that the variation of temperature or mass is small enough in a way that does not affect the velocity field, it is then considered that the scalar field is passively convected by the

†Email address for correspondence: t.yasuda.354@nitech.jp

velocity field. Such a scalar is sometimes called a 'passive scalar' and is the object of this study.

Heat and mass transport processes are controlled by the Prandtl number $Pr = \nu/\alpha$ and the Schmidt number $Sc = \nu/\kappa$, respectively, where ν is the kinematic viscosity, α is the thermal diffusivity and κ is the mass diffusivity. The Prandtl number takes a value of approximately 0.71 for air at atmospheric pressure and 27 °C, $Pr \approx 0.871$–13.6 for water (H_2O), $Pr \approx 100$–$50\,000$ for engine oils and $Pr \approx 0.003$–0.03 for liquid metals (Eckert & Drake 1959). The value of the Schmidt number, on the other hand, lies typically in the range of 0.2 to 4 for gas–gas diffusive systems at standard conditions, whereas $Sc \approx 200$–1500 for gas–liquid and liquid–liquid diffusive systems. Since both the Prandtl and Schmidt numbers range widely from small to large values in our surroundings, it is of great importance to clarify the parameter dependence of turbulent scalar transport over a broad range of the Schmidt number (or the Prandtl number).

It has been known that the statistical properties of passive scalar fluctuations transported by the turbulent velocity field vary significantly depending on the Reynolds number and Schmidt number. Such a variation is found, for example, in the scalar variance spectrum in homogeneous isotropic turbulence (see Gotoh, Watanabe & Suzuki 2011; Gotoh & Yeung 2012; Sreenivasan 2018). When the Reynolds number is sufficiently high, the asymptotic scalar variance spectrum has the form $k^{-17/3}$ in the inertial-diffusive range for $Sc \ll 1$, $k^{-5/3}$ in the inertial-convective range for $Sc = O(1)$, and k^{-1} in the viscous-convective range for $Sc \gg 1$ (Obukhov 1949; Corrsin 1951; Batchelor 1959; Batchelor, Howells & Townsend 1959). These power-law scalings have been studied extensively by early laboratory experiments (e.g., Sreenivasan 1996; Mydlarski & Warhaft 1998) and direct numerical simulations (DNS) (e.g., Watanabe & Gotoh 2004, 2007; Gotoh, Watanabe & Miura 2014; Yeung & Sreenivasan 2014; Gotoh & Watanabe 2015).

Since widely varying the Reynolds and Schmidt numbers results in the diversity of turbulently mixed states of a passive scalar and their corresponding statistics, it is meaningful to find a suitable control parameter upon which passive scalar statistics is systematically dependent, if any. The aim of this study is to demonstrate that the Péclet number based on the Taylor microscale of scalar fluctuation, defined in (2.15), works as such a control parameter. In passive scalar turbulence, there exist multiple characteristic length scales of velocity and scalar fluctuations. Having multiple choices of length scales, one can define the Péclet number using a characteristic length scale of velocity fluctuation (cf. (2.15)). Note here that characteristic length scales of scalar fluctuation vary relative to those of velocity fluctuation and the system size depending on the existing control parameters and injection methods of velocity and scalar fluctuations. Accounting for this variation may be one of the key ingredients to suitably characterise different turbulently mixed states of a passive scalar. One successful example of this is found in the work by Lepore & Mydlarski (2012), who investigated higher-order scalar structure functions for two different scalar fields generated in two ways: heated cylinder and mandoline. They found that, although the scalar (temperature) is convected by an identical turbulent flow, the value of the thermal integral length scale differs between heated cylinder and mandoline, which results in the different values of the Péclet number based on this length scale. When plotted against the Péclet-number-compensated separation, which takes into account the variation of the thermal integral length scale, the higher-order scalar structure functions collapse at small scales for the two different scalar fields (Lepore & Mydlarski 2012).

In this study, we investigate parameter dependencies of small-scale statistics of scalar fluctuations convected by statistically stationary homogeneous isotropic turbulence, considering the effect of variations of length scales of turbulence. Scalar fluctuations therein are sustained under a uniform mean scalar gradient. We focus especially on the small-scale anisotropy of scalar fluctuations appearing in this flow system. It has been reported that, in turbulent flows with a mean scalar gradient, the skewness of scalar derivative fluctuations in the direction of the mean gradient becomes non-zero (Sreenivasan & Tavoularis 1980; Budwig, Tavoularis & Corrsin 1985; Sreenivasan 1991; Holzer & Siggia 1994; Tong & Warhaft 1994; Mydlarski & Warhaft 1998; Warhaft 2000; Yeung, Xu & Sreenivasan 2002; Schumacher, Sreenivasan & Yeung 2003; Yeung *et al.* 2004; Yeung, Donzis & Sreenivasan 2005; Donzis & Yeung 2010; Yeung & Sreenivasan 2014), and it has still remained unsettled whether or not the small-scale scalar anisotropy can persist over a wide range of parameter values.

In order to achieve the aim mentioned above, we undertake an exhaustive parametric DNS study. We conduct DNS of passive scalar turbulence with 59 different combinations of Reynolds and Schmidt numbers. Since we change the values of these numbers herein, the velocity and scalar characteristic length scales vary accordingly although the scalar injection method is fixed. We discuss the parameter dependences of scalar statistics based on our DNS data. In § 2, we describe numerical methods and parameters used to simulate passive scalar turbulence. The results of the present study are shown in § 3, and our conclusion and discussion are presented in § 4.

2. Governing equations and numerical simulations

In the present study, we perform DNS of a passive scalar advected by statistically stationary homogeneous isotropic turbulence under a uniform mean scalar gradient. Under a triply periodic boundary condition ($0 \leqslant x_1, x_2, x_3 < 2\pi$), we solve the incompressible Navier–Stokes equations

$$\frac{\partial \boldsymbol{u}}{\partial t} + (\boldsymbol{u}\cdot\boldsymbol{\nabla})\boldsymbol{u} = -\frac{1}{\rho}\boldsymbol{\nabla} p + \nu\nabla^2\boldsymbol{u} + \boldsymbol{f}, \quad \boldsymbol{\nabla}\cdot\boldsymbol{u} = 0, \tag{2.1}$$

where $\boldsymbol{u}(\boldsymbol{x}, t)$, $p(\boldsymbol{x}, t)$ and $\boldsymbol{f}(\boldsymbol{x}, t)$ are the velocity, pressure and external forcing fields, respectively, and fluid density ρ is assumed to be constant. In order to generate statistically stationary isotropic turbulence, we use the white Gaussian isotropic force $\boldsymbol{f}(\boldsymbol{x}, t)$, which is defined in Fourier space as

$$\overline{\widehat{f}_i(\boldsymbol{k}, t)} = 0, \quad \overline{\widehat{f}_i(\boldsymbol{k}, t)\widehat{f}_j(-\boldsymbol{k}, s)} = P_{ij}(\boldsymbol{k})\frac{W(k)}{4\pi k^2}\delta(t-s), \tag{2.2a,b}$$

where $P_{ij}(\boldsymbol{k}) = \delta_{ij} - k_i k_j/k^2$ is a projection operator, δ_{ij} is the Kronecker delta, $\delta(\cdot)$ is the Dirac delta function and $\overline{(\cdot)}$ and $\widehat{(\cdot)}$ denote a time average and the Fourier coefficient of $(\cdot)$, respectively. Here, $W(k)$ is set to a constant value of 0.3 for the forcing wavenumber range $8 \leqslant |\boldsymbol{k}| \leqslant 9$, otherwise, $W(k) = 0$. With respect to a passive scalar, we decompose the scalar concentration $\Theta(\boldsymbol{x}, t)$ into mean and fluctuation parts as $\Theta(\boldsymbol{x}, t) = \overline{\Theta}(\boldsymbol{x}) + \theta(\boldsymbol{x}, t)$. For sustaining scalar fluctuations, we impose a uniform mean scalar gradient in the x_3-direction as $\boldsymbol{\nabla}\overline{\Theta} = (0, 0, \Gamma)$, where Γ is the magnitude of the gradient and is set to unity without loss of generality. We thereby solve the

following governing equation for $\theta(\boldsymbol{x}, t)$:

$$\frac{\partial}{\partial t}\theta + (\boldsymbol{u}\cdot\boldsymbol{\nabla})\theta = \kappa\nabla^2\theta - \Gamma u_3, \tag{2.3}$$

in conjunction with (2.1).

The energy spectrum, $E_u(k, t)$, is computed by integrating the energy spectral density $Q_u(\boldsymbol{k}, t) = \frac{1}{2}\widehat{u}_i(\boldsymbol{k}, t)\widehat{u}_i(-\boldsymbol{k}, t)$ over a spherical surface in $\boldsymbol{k}$-space as

$$E_u(k, t) = \int_0^{2\pi} \mathrm{d}\psi \int_0^{\pi} \mathrm{d}\phi k^2 \sin\phi Q_u(\boldsymbol{k}, t). \tag{2.4}$$

The scalar variance spectrum, $E_\theta(k, t)$, is similarly computed as

$$E_\theta(k, t) = \int_0^{2\pi} \mathrm{d}\psi \int_0^{\pi} \mathrm{d}\phi k^2 \sin\phi Q_\theta(\boldsymbol{k}, t), \tag{2.5}$$

where $Q_\theta(\boldsymbol{k}, t) = \widehat{\theta}(\boldsymbol{k}, t)\widehat{\theta}(-\boldsymbol{k}, t)$ is the scalar variance spectral density. Using these spectra, the total kinetic energy and scalar variance per unit mass are computed, respectively, as

$$\tfrac{1}{2}\langle\boldsymbol{u}^2\rangle(t) = \tfrac{3}{2}u'(t)^2 = \int_0^{\infty} E_u(k, t)\,\mathrm{d}k, \tag{2.6}$$

$$\langle\theta^2\rangle(t) = \theta'(t)^2 = \int_0^{\infty} E_\theta(k, t)\,\mathrm{d}k, \tag{2.7}$$

where $\langle(\cdot)\rangle$ denotes the space average of $(\cdot)$ over the entire computational domain, and $u'(t)$ and $\theta'(t)$ are the space-averaged root mean squares of velocity and scalar fluctuations.

Here we introduce several characteristic length scales of turbulence. We define integral length scales of velocity and scalar fluctuations, respectively, as

$$L_u(t) = \frac{3\pi}{4}\frac{\displaystyle\int_0^{\infty} k^{-1}E_u(k, t)\,\mathrm{d}k}{\displaystyle\int_0^{\infty} E_u(k, t)\,\mathrm{d}k}, \tag{2.8}$$

$$L_\theta(t) = \frac{\pi}{2}\frac{\displaystyle\int_0^{\infty} k^{-1}E_\theta(k, t)\,\mathrm{d}k}{\displaystyle\int_0^{\infty} E_\theta(k, t)\,\mathrm{d}k}. \tag{2.9}$$

The Taylor microscales of velocity and scalar fluctuations are computed, respectively, by

$$\lambda_u(t) = \sqrt{\frac{15\nu u'(t)^2}{\epsilon(t)}}, \tag{2.10}$$

$$\lambda_\theta(t) = \sqrt{\frac{6\kappa\theta'(t)^2}{\chi(t)}}, \tag{2.11}$$

where the energy dissipation rate $\epsilon(t)$ and the scalar dissipation rate $\chi(t)$ per unit mass are computed as $\epsilon(t) = \nu/2\langle(\partial u_i/\partial x_j + \partial u_j/\partial x_i)^2\rangle$ and $\chi(t) = 2\kappa\langle(\partial\theta/\partial x_i)^2\rangle$, respectively. The Kolmogorov scale, $\eta_K(t)$, and the Batchelor scale, $\eta_B(t)$, are defined as

$$\eta_K(t) = \nu^{3/4}\epsilon(t)^{-1/4}, \tag{2.12}$$

$$\eta_B(t) = \kappa^{1/2}\nu^{1/4}\epsilon(t)^{-1/4} = \eta_K(t)Sc^{-1/2}. \tag{2.13}$$

We discuss our results using the Reynolds number $Re_\lambda(t)$ based on $\lambda_u(t)$ and the Péclet number $Pe_{\lambda_\theta}(t)$ based on $\lambda_\theta(t)$, which are, respectively, written as

$$Re_\lambda(t) = \frac{u'(t)\lambda_u(t)}{\nu}, \tag{2.14}$$

$$Pe_{\lambda_\theta}(t) = \frac{u'(t)\lambda_\theta(t)}{\kappa}. \tag{2.15}$$

Instead of the Péclet number thus defined, $Pe_\lambda(t) = ScRe_\lambda(t) = u'(t)\lambda_u(t)/\kappa$ is sometimes used in the literature. As will be discussed, however, equation (2.15) is more appropriate in characterising the small-scale scalar statistics for various Reynolds and Schmidt numbers.

Setting moderate forcing wavenumbers ($8 \leqslant |\boldsymbol{k}| \leqslant 9$) in (2.2) effectively improves the isotropy of the velocity field. The $(2\pi)^3$ periodic domain becomes significantly larger than the integral length scale $\overline{L}_u$ of the velocity. See table 1 for the quantitative information about the isotropic flows of four different Reynolds numbers ($\overline{Re}_\lambda \approx 7$, 29, 63 and 106). Denoting one side of the triply periodic box by L_{box} ($=2\pi$), $L_{box}/\overline{L}_u$ is 22.2, 21.7, 27.2 and 29.6 at $\overline{Re}_\lambda \approx 7$, 29, 63 and 106, respectively. In this numerical set-up, a large number of eddies of various orientations, the size of which is comparable to $\overline{L}_u$, are contained in the computational domain, whereby even an instantaneous velocity field becomes reasonably isotropic on space average. Here, the degree of isotropy of velocity fluctuations is evaluated in terms of values of $\overline{u_2'^2}/\overline{u_1'^2}$ and $\overline{u_3'^2}/\overline{u_1'^2}$, both of which are very close to unity (thus velocity fluctuations being isotropic) for the four different Reynolds numbers (see table 1). One should keep in mind that, although the random forcing (2.2) is delta correlated in time, the velocity field has a finite correlation time of the order of T_L, where $T_L = \overline{L}_u/\overline{u'}$ is the large-eddy turnover time. Using larger forcing wavenumbers, we can reduce the effect of the finite correlation time such that it becomes shorter (relative to $L_{box}/\overline{u'}$) and the fluctuations of global quantities for velocity field are more attenuated. The latter is found in table 1 such that the ratio $\sigma_{u'^2}/\overline{u'^2}$ takes small values of the order of 10^{-2}, where $\sigma_{u'^2}$ is the temporal standard deviation of $u'(t)^2$. One of the important advantages of using moderate forcing wavenumbers is that it improves the sampling for small-scale statistics of scalar fluctuations albeit at the cost of a reduced inertial range. It also allows scalar structures to grow significantly larger than $\overline{L}_u$, as will be demonstrated in § 3.1. The velocity-derivative skewness $\overline{S}_u = \overline{\langle(\partial u_1/\partial x_1)^3\rangle/\langle(\partial u_1/\partial x_1)^2\rangle^{3/2}}$ is -0.00637, -0.342, -0.502 and -0.525 at $\overline{Re}_\lambda \approx 7$, 29, 63 and 106, respectively (table 1). The velocity field at $\overline{Re}_\lambda \approx 7$ is far from being turbulent. Nonetheless, the velocity field evolves in a spatio-temporally random manner because of the random forcing (2.2), thereby mixing a passive scalar.

In the present study, DNS is performed using the pseudo-spectral method and the fourth-order Runge–Kutta–Gill method (see Gotoh *et al.* (2011), for further details). We have run long-term numerical simulations at the four different Reynolds numbers

Label	ν	$\overline{Re}_\lambda$	$\overline{L}_u$	$\overline{\lambda}_u$	$\overline{\eta}_K$	$\overline{u_2'^2}/\overline{u_1'^2}$	$\overline{u_3'^2}/\overline{u_1'^2}$	$\sigma_{u'^2}/\overline{u'^2}$	$\overline{S}_u$
A	0.01	7.23	0.283	0.264	0.0419	1.001	0.9994	0.0540	−0.00637
B	0.003	29.0	0.289	0.215	0.0171	0.9995	0.9978	0.0390	−0.342
C	8×10^{-4}	62.7	0.231	0.117	0.00633	1.002	1.004	0.0285	−0.502
D	3×10^{-4}	106	0.212	0.0726	0.00301	1.001	0.9984	0.0282	−0.525

TABLE 1. Velocity statistics of DNS with the four different values of ν. Here, Re_λ is the Reynolds number based on the Taylor microscale (2.14), L_u is the integral length scale (2.8), λ_u is the Taylor microscale (2.10), η_K is the Kolmogorov microscale (2.12), S_u is the velocity-derivative skewness. The velocity statistics of labels A, B, C and D are, respectively, computed using runs A1, B1, C1 and D1 shown in tables 2 and 3.

($\overline{Re}_\lambda \approx 7,\ 29,\ 63,\ 106$) while varying the Schmidt number. We use 59 different combinations of ν and Sc, where the lowest and highest Sc used are 1/4096 and 256, respectively (see tables 2 and 3). When $Sc \ll 1$, it is necessary to make the time resolution finer to resolve the scalar diffusion time scale that becomes much shorter than the advection time scales. We also need to allocate the number of numerical grid points, N^3, such that both the Kolmogorov scale (2.12) and the Batchelor scale (2.13) are well resolved. When Sc is unity, the Kolmogorov scale equals the Batchelor scale (i.e., $\overline{\eta}_K = \overline{\eta}_B$). At a fixed Reynolds number, however, $\overline{\eta}_B$ becomes smaller with increasing Sc so that N^3 must be increased accordingly (Yeung *et al.* 2004; Donzis & Yeung 2010; Gotoh, Hatanaka & Miura 2012). In the present study, we use a reasonable spatial resolution for each simulation; $k_{max}\overline{\eta}_B$ is at worse equal to 1.24 for run A256 (see table 2), where the cutoff wavenumber $k_{max} = \sqrt{2}N/3$ (Gotoh & Yeung 2012). For computing turbulence statistics in a statistically stationary state, time averages are taken over the time period of T_{av} which excludes the initial transient period of time. Here, T_{av} is at worse equal to 4.19 T_L for run D1024i (see table 3).

3. Results

3.1. *Scalar variance spectra and flow visualisations*

Figure 1(*a*) shows the variation of the time-averaged scalar variance spectrum $\overline{E}_\theta(k)$ for decreasing Sc at the highest Reynolds number $\overline{Re}_\lambda \approx 106$. Here, $\overline{E}_\theta(k)$ exhibits the power-law scalings slightly shallower than $k^{-5/3}$ for $Sc = 1$ and than $k^{-17/3}$ for $Sc = 1/1024$ (Yeung & Sreenivasan 2013, 2014). Batchelor *et al.* (1959) analytically derived the $k^{-17/3}$ power-law scaling for the turbulent scalar fluctuation field, which is locally isotropic. We show below, however, the case in which the scalar fluctuation field is significantly anisotropic when the power-law scaling slightly shallower than $k^{-17/3}$ emerges in the scalar variance spectrum. There is a peculiar tendency that, at $Sc = 1/1024$, $\overline{E}_\theta(k)$ increases significantly with decreasing k for $k \leqslant 7$. This tendency is partially described by the shape of the energy spectrum at $\overline{Re}_\lambda \approx 106$. Figure 1(*b*) shows $\overline{E}_u(k)$ and multiplied energy spectrum $k^{-4}\overline{E}_u(k)$ at $\overline{Re}_\lambda \approx 106$. Note that Batchelor *et al.* (1959) theoretically derived $\overline{E}_\theta(k) = (\chi/3\kappa^3)k^{-4}\overline{E}_u(k)$ for $Sc \ll 1$. Here, $k^{-4}\overline{E}_u(k)$ is an increasing function with decreasing k for $k \leqslant 7$, as similarly observed in $\overline{E}_\theta(k)$. Therefore, for $Sc \ll 1$, the scalar variance spectrum $\overline{E}_\theta(k)$ can be related to the multiplied energy spectrum $k^{-4}\overline{E}_u(k)$. Incidentally, we find that the velocity-scalar cospectrum shows the power-law scaling slightly shallower than $k^{-11/3}$ in the inertial-diffusive range at low Schmidt numbers and $\overline{Re}_\lambda \approx 106$ (data not shown). The $k^{-11/3}$ power-law scaling was theoretically derived by O'Gorman & Pullin (2005).

Run	ν	Sc	N^3	Δt	$\overline{Pe}_{\lambda_\theta}$	$\overline{S}_{\partial\theta/\partial x_3}$	$\overline{F}_{\partial\theta/\partial x_3}$	$\overline{g}_\theta$	$\overline{a}$	$k_{max}\overline{\eta}_B$	T_{av}
A1	0.01	1	256^3	0.01	5.98	1.08	5.05	0.981	0.206	5.05	222
A2i	0.01	1/2	256^3	0.009	3.44	0.873	4.25	0.816	0.370	7.15	218
A4i	0.01	1/4	256^3	0.0045	2.53	0.622	3.60	0.650	0.621	10.1	126
A8i	0.01	1/8	256^3	0.0023	1.55	0.403	3.23	0.539	0.842	14.3	83.2
A16i	0.01	1/16	256^3	0.0011	0.736	0.231	3.07	0.496	0.952	20.2	269
A32i	0.01	1/32	256^3	5.7×10^{-4}	0.403	0.121	3.01	0.475	0.987	28.6	186
A64i	0.01	1/64	256^3	2.8×10^{-4}	0.180	0.0598	3.00	0.471	0.997	40.4	89.4
A128i	0.01	1/128	256^3	1.4×10^{-4}	0.0942	0.0439	3.01	0.477	0.999	57.1	35.2
A256i	0.01	1/256	256^3	7.1×10^{-5}	0.0465	0.0201	2.99	0.474	0.9998	80.2	19.9
A2	0.01	2	256^3	0.01	10.1	1.23	6.01	1.07	0.123	3.57	213
A4	0.01	4	256^3	0.01	16.5	1.30	6.96	1.11	0.0846	2.53	300
A8	0.01	8	256^3	0.01	27.2	1.27	7.76	1.10	0.0548	1.79	213
A16	0.01	16	256^3	0.01	42.3	1.13	8.11	1.08	0.0367	1.27	213
A32	0.01	32	512^3	0.003	65.9	1.02	8.83	1.05	0.0211	1.79	67.7
A64	0.01	64	512^3	0.003	102	0.835	8.97	1.01	0.00768	1.27	67.7
A128	0.01	128	1024^3	0.001	156	0.646	9.22	1.05	0.0190	1.79	11.6
A256	0.01	256	1024^3	0.001	242	0.524	9.53	1.03	0.00971	1.24	13.5
B1	0.003	1	256^3	0.01	17.9	1.52	8.87	1.13	0.0724	2.06	309
B2i	0.003	1/2	256^3	0.01	11.2	1.45	7.68	1.10	0.0993	2.90	309
B4i	0.003	1/4	256^3	0.01	7.13	1.29	6.41	1.03	0.151	4.10	309
B8i	0.003	1/8	256^3	0.0076	4.30	1.07	5.26	0.879	0.267	5.81	241
B16i	0.003	1/16	256^3	0.0038	2.91	0.830	4.35	0.712	0.491	8.20	149
B32i	0.003	1/32	256^3	0.0019	1.75	0.588	3.62	0.585	0.757	11.6	67.3
B64i	0.003	1/64	256^3	9.5×10^{-4}	0.928	0.404	3.27	0.521	0.918	16.4	54.7
B128i	0.003	1/128	256^3	4.7×10^{-4}	0.534	0.269	3.12	0.499	0.977	23.1	137
B256i	0.003	1/256	256^3	2.4×10^{-4}	0.250	0.174	3.04	0.495	0.994	32.8	115
B512i	0.003	1/512	256^3	1.2×10^{-4}	0.133	0.142	3.04	0.487	0.998	46.4	40.4
B1024i	0.003	1/1024	256^3	5.9×10^{-5}	0.0652	0.129	3.02	0.492	0.9996	64.5	28.7
B2	0.003	2	256^3	0.01	27.7	1.43	9.53	1.11	0.0512	1.45	309
B4	0.003	4	512^3	0.005	43.0	1.36	10.8	1.09	0.0373	2.05	161
B8	0.003	8	512^3	0.005	65.8	1.14	10.9	1.07	0.0252	1.46	160
B16	0.003	16	1024^3	0.002	101	0.972	11.5	1.05	0.0197	2.06	30.9
B32	0.003	32	1024^3	0.002	153	0.759	11.4	1.04	0.0133	1.46	36.5

TABLE 2. Parameters and scalar statistics of DNS with various values of Sc for $\nu = 0.01$ (series-A) and 0.003 (series-B). Here, ν is the kinematic viscosity, Sc is the Schmidt number, N^3 is the number of numerical grid points, Δt is the time increment, Pe_{λ_θ} is the Péclet number based on the Taylor microscale of scalar fluctuation (2.15), $S_{\partial\theta/\partial x_3}$ is the scalar derivative skewness (3.1), $F_{\partial\theta/\partial x_3}$ is the scalar derivative flatness (3.2), g_θ is the ratio of parallel-to-perpendicular scalar-gradient variances (3.3), a is the anisotropy parameter (3.4), $k_{max}\eta_B$ is the spatial resolution, T_{av} is the time period for computing statistics in the unit of large-eddy turnover time, T_L.

Figure 2 shows the visualisations of the instantaneous enstrophy and scalar fluctuation fields with three different Schmidt numbers ($Sc = 1,\ 1/64,\ 1/1024$), at $\overline{Re}_\lambda \approx 106$. We find an interesting feature that scalar fluctuation structures visualised by cyan isosurfaces become larger for decreasing Sc. At the lowest Schmidt number ($Sc = 1/1024$), anomalous large-scale anisotropic scalar structures emerge from the isotropic turbulent velocity field (figure 2*c*). These structures are elongated along the direction of the mean scalar gradient, and their size is significantly large

Run	ν	Sc	N^3	Δt	$\overline{Pe}_{\lambda_\theta}$	$\overline{S}_{\partial\theta/\partial x_3}$	$\overline{F}_{\partial\theta/\partial x_3}$	$\overline{g}_\theta$	$\overline{a}$	$k_{max}\overline{\eta}_B$	T_{av}
C1	8×10^{-4}	1	512^3	0.005	34.6	1.59	12.4	1.11	0.0450	1.53	203
C2i	8×10^{-4}	1/2	512^3	0.005	22.8	1.70	11.6	1.12	0.0575	2.16	203
C4i	8×10^{-4}	1/4	512^3	0.005	15.0	1.67	10.1	1.11	0.0768	3.05	314
C8i	8×10^{-4}	1/8	512^3	0.003	9.68	1.52	8.40	1.06	0.107	4.32	129
C16i	8×10^{-4}	1/16	512^3	0.003	6.50	1.30	6.81	0.962	0.170	6.09	129
C32i	8×10^{-4}	1/32	512^3	0.0018	3.94	1.05	5.37	0.815	0.320	8.63	85.0
C64i	8×10^{-4}	1/64	512^3	8.9×10^{-4}	2.50	0.798	4.31	0.663	0.573	12.2	69.8
C128i	8×10^{-4}	1/128	512^3	4.4×10^{-4}	1.66	0.562	3.60	0.561	0.815	17.3	25.5
C256i	8×10^{-4}	1/256	512^3	2.2×10^{-4}	0.912	0.366	3.23	0.502	0.941	24.4	19.6
C512i	8×10^{-4}	1/512	512^3	1.1×10^{-4}	0.440	0.257	3.13	0.500	0.984	34.1	27.4
C1024i	8×10^{-4}	1/1024	512^3	5.5×10^{-5}	0.200	0.184	3.09	0.499	0.996	47.5	12.2
C2048i	8×10^{-4}	1/2048	512^3	2.8×10^{-5}	0.154	0.121	3.03	0.464	0.999	63.3	12.9
C4096i	8×10^{-4}	1/4096	512^3	1.4×10^{-5}	0.0742	0.130	3.04	0.498	0.9996	82.6	8.37
C2	8×10^{-4}	2	1024^3	0.002	54.5	1.46	13.7	1.09	0.0337	2.15	38.8
C4	8×10^{-4}	4	1024^3	0.002	79.9	1.22	13.7	1.07	0.0251	1.53	38.8
D1	3×10^{-4}	1	1024^3	0.002	57.0	1.57	15.6	1.09	0.0338	1.45	26.8
D2i	3×10^{-4}	1/2	1024^3	0.002	38.5	1.79	15.2	1.11	0.0434	2.06	35.0
D4i	3×10^{-4}	1/4	1024^3	0.002	26.1	1.85	13.8	1.12	0.0530	2.93	32.9
D8i	3×10^{-4}	1/8	1024^3	0.002	17.6	1.78	11.8	1.10	0.0650	4.13	39.1
D16i	3×10^{-4}	1/16	1024^3	0.0012	13.7	1.61	9.62	1.07	0.0877	5.83	119
D32i	3×10^{-4}	1/32	1024^3	0.0012	9.94	1.37	7.56	0.988	0.133	8.27	131
D64i	3×10^{-4}	1/64	1024^3	5.9×10^{-4}	6.15	1.15	5.96	0.881	0.239	11.3	55.8
D128i	3×10^{-4}	1/128	1024^3	3×10^{-4}	3.77	0.888	4.65	0.736	0.447	15.6	29.8
D256i	3×10^{-4}	1/256	1024^3	1.5×10^{-4}	2.64	0.684	3.96	0.611	0.674	20.8	18.7
D512i	3×10^{-4}	1/512	1024^3	7.4×10^{-5}	1.75	0.507	3.51	0.554	0.839	25.3	11.8
D1024i	3×10^{-4}	1/1024	1024^3	3.7×10^{-5}	1.06	0.345	3.20	0.464	0.951	35.6	4.19

TABLE 3. Parameters and scalar statistics of DNS with various values of Sc for $\nu = 8\times10^{-4}$ (series-C) and 3×10^{-4} (series-D). The description of the parameters and statistics shown is found in the caption of table 2.

(cf. Schumacher, Sreenivasan & Yeung 2005). This size is visually evident by comparison with the size of the red cube at the right-hand bottom corner, one side of which is $\overline{L}_u$ (figure 2*c*). Quantitative evidence for this is shown in figure 3 in terms of the variations of $\overline{L}_\theta/\overline{L}_u$ and $\overline{\lambda}_\theta/\overline{L}_u$ with respect to $\overline{Pe}_{\lambda_\theta}$. In accordance with our visualisation (figure 2), the scalar characteristic length scales $\overline{L}_\theta$ and $\overline{\lambda}_\theta$ increase compared to $\overline{L}_u$ with decreasing $\overline{Pe}_{\lambda_\theta}$. For $\overline{Re}_\lambda \approx 106$, $\overline{L}_\theta/\overline{L}_u$ and $\overline{\lambda}_\theta/\overline{L}_u$ reach approximately 6 and 2.5, respectively, at $\overline{Pe}_{\lambda_\theta} = 1.06$. Overall, similar variations of $\overline{L}_\theta/\overline{L}_u$ and $\overline{\lambda}_\theta/\overline{L}_u$ with respect to $\overline{Pe}_{\lambda_\theta}$ are confirmed for all the Reynolds numbers shown ($\overline{Re}_\lambda \approx 7$, 29, 63, 106). Note that, as seen in figure 2, we confirm a similar change of a scalar fluctuation field for decreasing Sc and $\overline{Pe}_{\lambda_\theta}$ at $\overline{Re}_\lambda \approx 7$, 29, 63. Moreover, it is worth mentioning that no spontaneous formation of large-scale anisotropic scalar structures is identified when applying a white Gaussian scalar source (see Watanabe & Gotoh (2004), for details) instead of the uniform mean scalar gradient. This implies that the mean gradient is one of the key ingredients for the generation and sustenance of the large-scale anisotropic scalar structures (figure 2*c*).

Here, the formation mechanism of the large-scale scalar structures when $Sc \ll 1$ is explained as follows. First, blobs of mean scalar with amplitude of $O(\Gamma L_f)$, where $L_f = 2\pi/k_f$ and k_f is the characteristic wavenumber of the forcing, are convected in

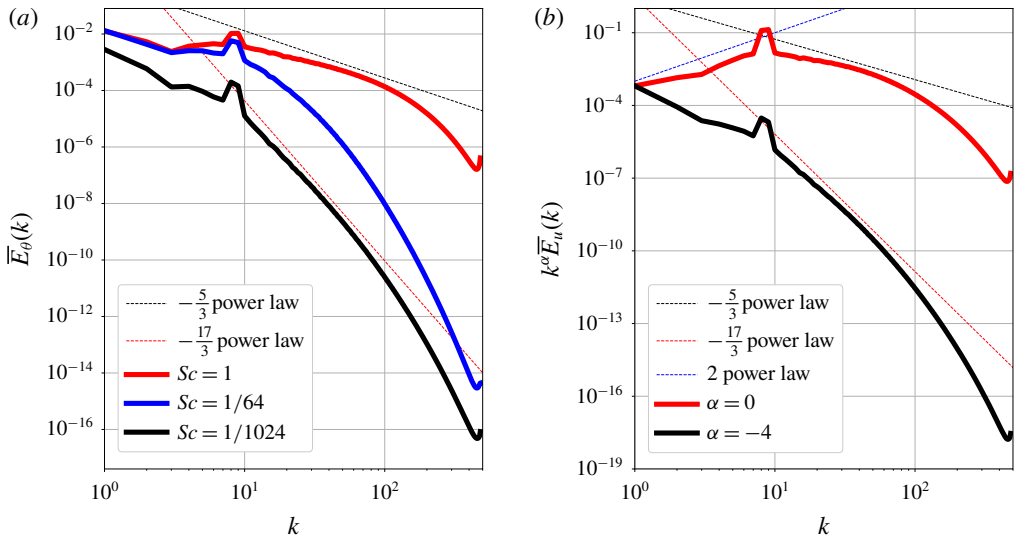

FIGURE 1. (*a*) Time-averaged scalar variance spectra $\overline{E}_\theta(k)$ with three different Schmidt numbers at $\overline{Re}_\lambda \approx 106$. The red, blue and black curves correspond to $Sc = 1$, $1/64$ and $1/1024$, respectively. (*b*) Time-averaged energy spectra $k^\alpha \overline{E}_u(k)$, at $\overline{Re}_\lambda \approx 106$. The red and black curves correspond to $\alpha = 0$ and $\alpha = -4$, respectively. The dashed black, red and blue lines denote the $k^{-5/3}$, $k^{-17/3}$ and k^2 power-law slopes, respectively.

the direction parallel to the mean scalar gradient by the velocity fluctuations of the scale $\overline{L}_u = O(L_f)$. Once the convected scalar blobs meet, they quickly merge into larger blobs due to the large diffusivity with the time scale of L_f^2/κ ($\ll \overline{L}_u/\overline{u'} = T_L$). Note that the fluid blobs do not merge due to the incompressibility. The convection and merging process of the scalar continue successively and selectively in the direction parallel to the mean scalar gradient, resulting in the formation of large-scale anisotropic scalar structures elongated in the direction of the mean gradient (figure 2*c*).

3.2. *Dependences of scalar derivative statistics on Sc and* $\overline{Pe}_{\lambda_\theta}$

In figure 4, we show the well known scalar derivative statistics: the scalar derivative skewness and flatness, both of which have been investigated in the literature (Sreenivasan & Tavoularis 1980; Budwig *et al.* 1985; Sreenivasan 1991; Holzer & Siggia 1994; Tong & Warhaft 1994; Mydlarski & Warhaft 1998; Warhaft 2000; Yeung *et al.* 2002; Schumacher *et al.* 2003; Yeung *et al.* 2004, 2005; Donzis & Yeung 2010; Yeung & Sreenivasan 2014). In the present study, we compute the instantaneous skewness and flatness of $\partial\theta/\partial x_3$, respectively, as

$$S_{\partial\theta/\partial x_3}(t) = \left\langle \left(\frac{\partial\theta}{\partial x_3} - \left\langle \frac{\partial\theta}{\partial x_3} \right\rangle \right)^3 \right\rangle \Bigg/ \left\langle \left(\frac{\partial\theta}{\partial x_3} - \left\langle \frac{\partial\theta}{\partial x_3} \right\rangle \right)^2 \right\rangle^{3/2}, \tag{3.1}$$

$$F_{\partial\theta/\partial x_3}(t) = \left\langle \left(\frac{\partial\theta}{\partial x_3} - \left\langle \frac{\partial\theta}{\partial x_3} \right\rangle \right)^4 \right\rangle \Bigg/ \left\langle \left(\frac{\partial\theta}{\partial x_3} - \left\langle \frac{\partial\theta}{\partial x_3} \right\rangle \right)^2 \right\rangle^2. \tag{3.2}$$

In all the parameter cases, we confirm that both $S_{\partial\theta/\partial x_3}(t)$ and $F_{\partial\theta/\partial x_3}(t)$ fluctuate around their most probable values beyond the initial transient period of time.

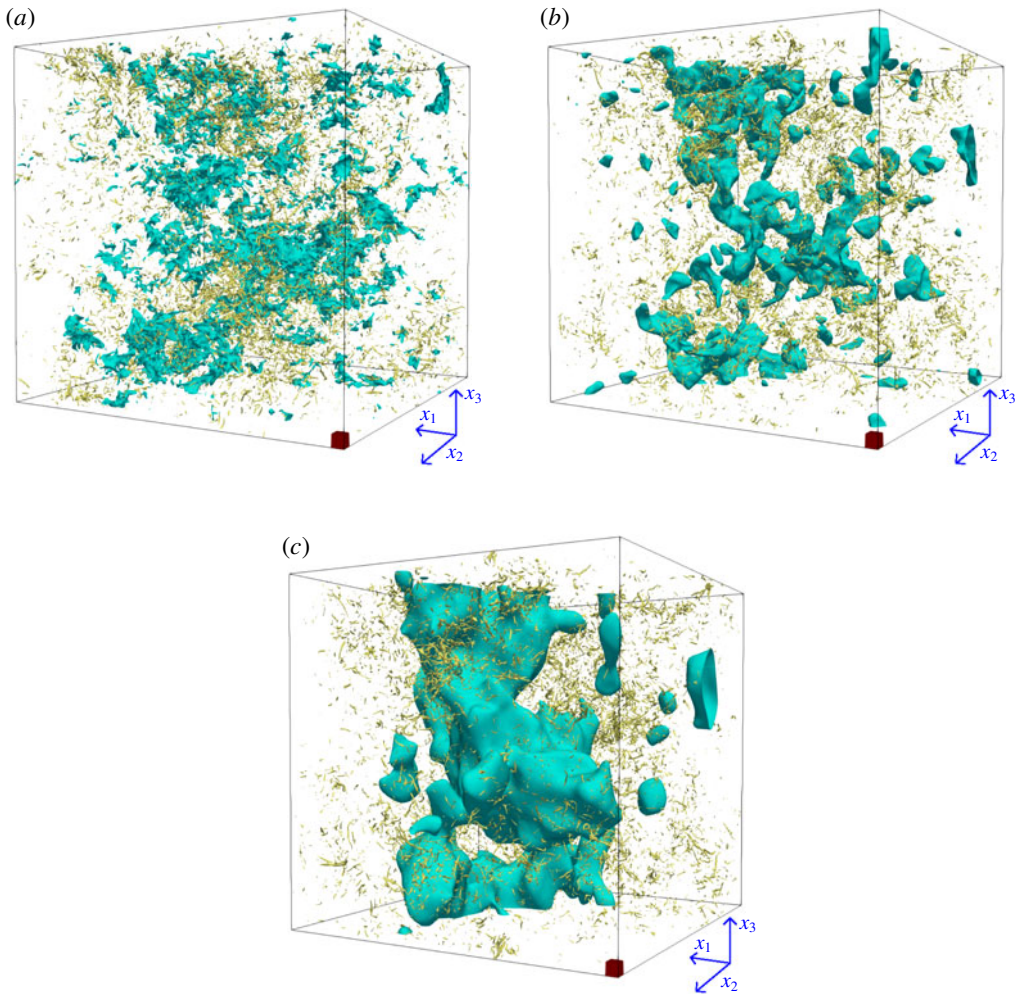

FIGURE 2. Visualisations of instantaneous flow fields of passive scalar turbulence with a uniform mean scalar gradient. Yellow isosurfaces denote high enstrophy. Cyan isosurfaces denote scalar fluctuation ($\theta < 0$). Here, $\overline{Re}_\lambda \approx 106$. One side of the small red cube placed in the bottom right-hand corner of the periodic domain is the integral length scale $\overline{L}_u$ of velocity fluctuation. (*a*) Run D1, $Sc = 1$ and $\overline{Pe}_{\lambda_\theta} = 57.0$; (*b*) run D64i, $Sc = 1/64$ and $\overline{Pe}_{\lambda_\theta} = 6.15$; (*c*) run D1024i, $Sc = 1/1024$ and $\overline{Pe}_{\lambda_\theta} = 1.06$.

Figures 4(*a*1) and 4(*b*1) demonstrate the dependences of $\overline{S}_{\partial\theta/\partial x_3}$ and $\overline{F}_{\partial\theta/\partial x_3}$ on Sc, respectively, alongside the published data by Yeung *et al.* (2002, 2004). Our data and the published data of multiple $\overline{Re}_\lambda$ demonstrate a qualitatively similar tendency. As Sc is increased from a very low value, $\overline{S}_{\partial\theta/\partial x_3}$ first monotonically increases, and then decreases after reaching a peak (figure 4*a*1). Another important observation from figure 4(*a*1) is that, at $Sc = 1$, $\overline{S}_{\partial\theta/\partial x_3}$ takes almost the same value ($\approx$1.5) at $\overline{Re}_\lambda$, greater than or equal to 29. This observation is relevant to the persistence of non-zero derivative skewness of a passive scalar (Sreenivasan 1991; Tong & Warhaft 1994; Mydlarski & Warhaft 1998). The experiments of grid turbulence under a mean temperature gradient (Tong & Warhaft 1994; Mydlarski & Warhaft 1998) demonstrated

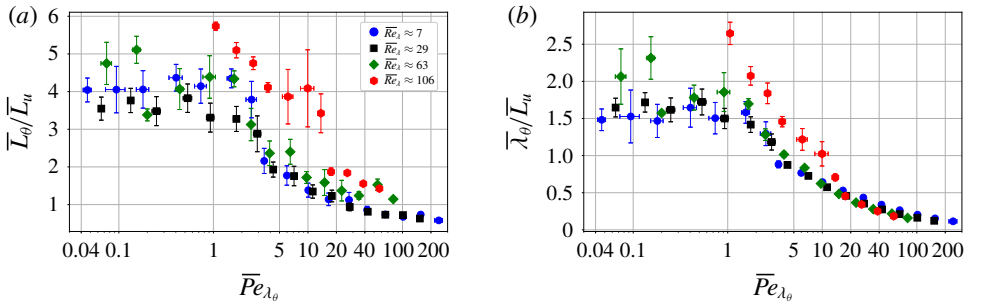

FIGURE 3. The $\overline{Pe}_{\lambda_\theta}$-dependences of $\overline{L}_\theta/\overline{L}_u$ (*a*) and $\overline{\lambda}_\theta/\overline{L}_u$ (*b*). Blue circles, black squares, green diamonds and red hexagons indicate the data for $\overline{Re}_\lambda \approx 7$, 29, 63 and 106, respectively. Horizontal error bars denote the temporal standard deviations of $Pe_{\lambda_\theta}(t)$ and vertical error bars denote those of $L_\theta(t)/\overline{L}_u$ (*a*) and $\lambda_\theta(t)/\overline{L}_u$ (*b*). Both $\overline{L}_\theta/\overline{L}_u$ and $\overline{\lambda}_\theta/\overline{L}_u$ show near constancy in the low Péclet number range because the scalar structures stop growing in size due to the domain size limit.

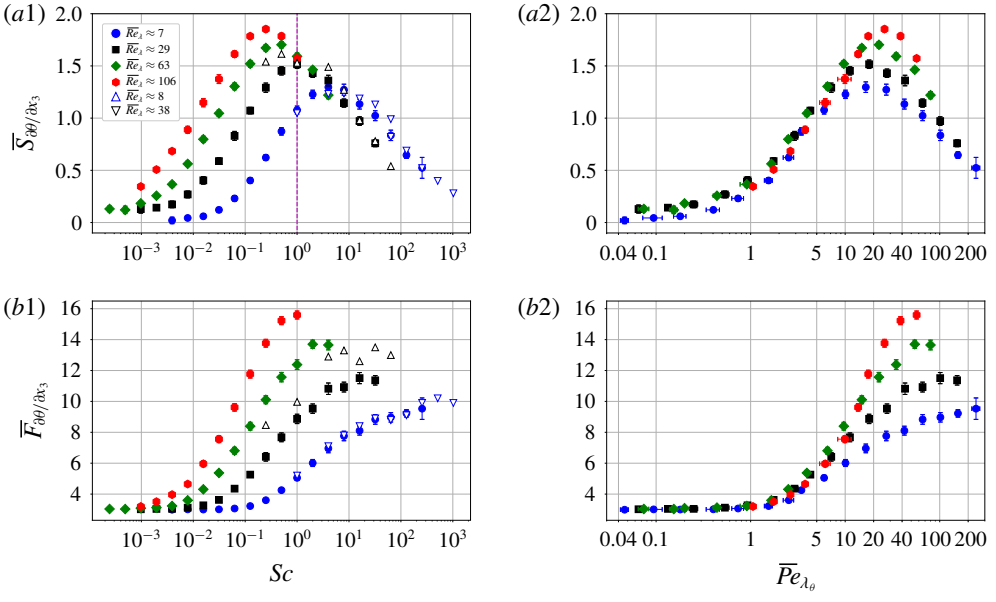

FIGURE 4. Skewness (*a*1,*a*2) and flatness (*b*1,*b*2) of scalar derivative $\partial\theta/\partial x_3$ as functions of Sc (*a*1,*b*1) and $\overline{Pe}_{\lambda_\theta}$ (*a*2,*b*2). Blue circles, black squares, green diamonds and red hexagons indicate the data for $\overline{Re}_\lambda \approx 7$, 29, 63 and 106, respectively. (*a*1,*b*1) Open blue inverted triangles, $\overline{Re}_\lambda \approx 8$ from Yeung *et al.* (2004); open black triangles, $\overline{Re}_\lambda \approx 38$ from Yeung *et al.* (2002). (*a*2) Here, $\overline{S}_{\partial\theta/\partial x_3}$ becomes maximal at $\overline{Pe}_{\lambda_\theta} \approx 20$ at each Reynolds number. Horizontal and vertical error bars denote the temporal standard deviations of the corresponding quantities.

that the temperature derivative skewness takes a constant value of approximately 1.4 over a broad range of Reynolds number (up to $\overline{Re}_\lambda \approx 731$), with the Prandtl number (or Sc) being of order unity. $\overline{F}_{\partial\theta/\partial x_3}$ is, on the other hand, a monotonically increasing function of Sc for each Reynolds number (figure 4*b*1). The increase rate in $\overline{F}_{\partial\theta/\partial x_3}$ is observed to grow with increasing $\overline{Re}_\lambda$.

Next, we compare plots of $\overline{S}_{\partial\theta/\partial x_3}$ with respect to Sc and $\overline{Pe}_{\lambda_\theta}$ (figures 4*a*1 and 4*a*2). Although the variations of $\overline{S}_{\partial\theta/\partial x_3}$ with respect to Sc do not collapse for different $\overline{Re}_\lambda$ (figure 4*a*1), when plotted with respect to $\overline{Pe}_{\lambda_\theta}$ the variations collapse well in the low $\overline{Pe}_{\lambda_\theta}$ range (figure 4*a*2). We also confirm the dependence of $\overline{F}_{\partial\theta/\partial x_3}$ on $\overline{Pe}_{\lambda_\theta}$ (figure 4*b*2). At much higher $\overline{Pe}_{\lambda_\theta}$ than unity, the plots with respect to $\overline{Pe}_{\lambda_\theta}$ for different $\overline{Re}_\lambda$ do not collapse onto each other (see figure 4*b*2). In other words, the spatio-temporal intermittency of scalar fluctuations is sensitive to $\overline{Re}_\lambda$ for $\overline{Pe}_{\lambda_\theta} \gg 1$. The good agreement of plots for the four different $\overline{Re}_\lambda$ in the low $\overline{Pe}_{\lambda_\theta}$ range is due to the decoupling effect between velocity and scalar fluctuation fields, which is assessed in terms of mixed spectral skewness in § 3.4.

3.3. $\overline{Pe}_{\lambda_\theta}$-dependence of small-scale anisotropy of scalar fluctuations

In order to evaluate the degree of small-scale anisotropy of scalar fluctuations, we compute the ratio of parallel-to-perpendicular scalar-gradient variances, $g_\theta(t)$, defined as

$$g_\theta(t) = 2\left\langle \frac{\partial\theta}{\partial x_3}\frac{\partial\theta}{\partial x_3}\right\rangle \Big/ \left[\left\langle \frac{\partial\theta}{\partial x_1}\frac{\partial\theta}{\partial x_1}\right\rangle + \left\langle \frac{\partial\theta}{\partial x_2}\frac{\partial\theta}{\partial x_2}\right\rangle\right]. \tag{3.3}$$

Such a quantity has also been studied in the literature (Tong & Warhaft 1994; Mydlarski & Warhaft 1998; Yeung & Sreenivasan 2014; Hill 2017).

We also use the anisotropy parameter $a(t)$ proposed by Hill (2017), defined as

$$a(t) = \frac{F(t) + \dfrac{\kappa}{\kappa_T(t)}}{1 + \dfrac{\kappa}{\kappa_T(t)}}, \tag{3.4}$$

where $F(t)$ is defined as

$$F(t) = \frac{g_\theta(t) - 1}{g_\theta(t) + 2}, \tag{3.5}$$

and $\kappa/\kappa_T(t)$ is calculated using the eddy diffusivity $\kappa_T(t) = \chi(t)/2\Gamma^2$ by

$$\frac{\kappa}{\kappa_T(t)} = \frac{2\kappa\Gamma^2}{\chi(t)} = \Gamma^2 \Big/ \left\langle \frac{\partial\theta}{\partial x_i}\frac{\partial\theta}{\partial x_i}\right\rangle = \frac{\partial\Theta}{\partial x_3}\frac{\partial\Theta}{\partial x_3} \Big/ \left\langle \frac{\partial\theta}{\partial x_i}\frac{\partial\theta}{\partial x_i}\right\rangle. \tag{3.6}$$

Both $g_\theta(t)$ and $F(t)$ relate to the small-scale anisotropy of scalar fluctuations, whereas $\kappa/\kappa_T(t)$ measures the macroscopic effect of the mean scalar gradient on scalar fluctuations. If small-scale scalar fluctuations become statistically isotropic, then $\overline{g}_\theta = 1$ and $\overline{F} = 0$ (note, however, that the opposite is not necessarily the case). The eddy diffusivity, $\kappa_T(t)$, measures the strength of scalar mixing. The enhancement of mixing a passive scalar, therefore, results in the increase of $\kappa_T(t)$ relative to κ, i.e., the decrease of $\kappa/\kappa_T(t)$. One may expect that, when $\kappa/\kappa_T(t)$ is small, small-scale scalar fluctuations are isotropised due to the effective scalar mixing by the background isotropic flow. When $\kappa/\kappa_T(t)$ is large, on the other hand, small-scale gradients of scalar field do not develop but the strong molecular diffusion is balanced by the scalar excitations due to velocity fluctuations in the direction of the mean scalar gradient, wherein large-scale anisotropic scalar structures are

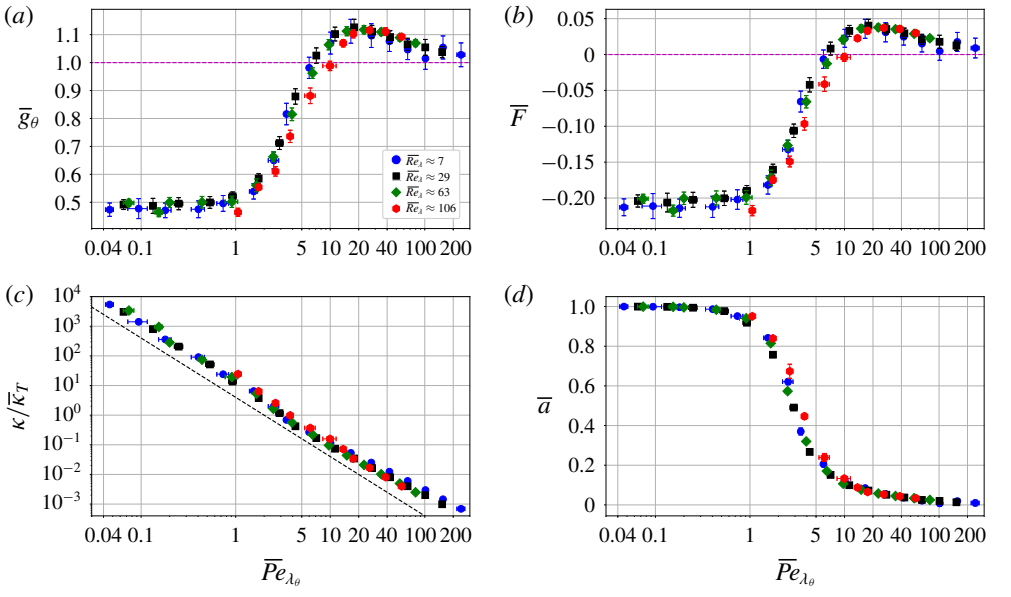

FIGURE 5. The $\overline{Pe}_{\lambda_\theta}$-dependences of (*a*) $\overline{g}_\theta$, (*b*) $\overline{F}$, (*c*) $\kappa/\overline{\kappa}_T$ and (*d*) $\overline{a}$. Blue circles, black squares, green diamonds and red hexagons indicate data for $\overline{Re}_\lambda \approx 7$, 29, 63 and 106, respectively. Horizontal and vertical error bars denote the temporal standard deviations of the corresponding quantities. (*c*) The black dashed line shows $\kappa/\overline{\kappa}_T \propto \overline{Pe}_{\lambda_\theta}^{-2}$ (see appendix A for the derivation of the power-law scaling).

formed (figure 2*c*). Here, $F(t)$ and $\kappa/\kappa_T(t)$ are contained in the anisotropic parameter $a(t)$ (3.4), where $a(t)$ is a measure of the ratio of the second-order coefficient (with a minus sign) to the zero-order coefficient in the Legendre expansion of shell-summed scalar variance spectral density (see Hill (2017), for details). When $\kappa/\kappa_T(t) \gg |F(t)|$ and $\kappa/\kappa_T(t) \gg 1$, both numerator and denominator of $a(t)$ are approximately equal to $\kappa/\kappa_T(t)$, which yields $a(t) \approx 1$; in other words, the second-order contribution in the Legendre expansion becomes almost as significant as the zero-order one. The scalar fluctuation field accordingly becomes an axisymmetric field that is highly affected by the mean scalar gradient (Hill 2017).

Figure 5 illustrates $\overline{Pe}_{\lambda_\theta}$-dependences of time-averaged values of the quantities introduced above (i.e., $\overline{g}_\theta$, $\overline{F}$, $\kappa/\overline{\kappa}_T$, $\overline{a}$). The plots of $\overline{g}_\theta$ and $\overline{F}$ for the four different $\overline{Re}_\lambda$ collapse well onto a single curve when arranged in terms of $\overline{Pe}_{\lambda_\theta}$ (see figures 5*a* and 5*b*). There is a zero-crossing point of the curve of $\overline{F}$ at $\overline{Pe}_{\lambda_\theta} \approx 7$. Below $\overline{Pe}_{\lambda_\theta} \approx 7$, the scalar gradient fluctuations in the direction of the mean scalar gradient (i.e., vertical direction) become weaker than those in the directions perpendicular to it (horizontal directions), whereas those in the vertical direction become stronger than those in the horizontal directions above $\overline{Pe}_{\lambda_\theta} \approx 7$. Above $\overline{Pe}_{\lambda_\theta} \approx 20$, where $\overline{g}_\theta$ and $\overline{F}$ take their local maximal values, the dissipation-scale scalar fluctuations become less anisotropic with increasing $\overline{Pe}_{\lambda_\theta}$, irrespective of $\overline{Re}_\lambda$. As $\overline{Pe}_{\lambda_\theta}$ increases, the effect of turbulent scalar mixing becomes more significant. Consequently, turbulent scalar mixing isotropises scalar fluctuations at dissipative scales.

In figures 5(*a*) and 5(*b*), we find that $\overline{g}_\theta$ and $\overline{F}$ approach the values of 0.5 and -0.2, respectively, in the limit of $\overline{Pe}_{\lambda_\theta} \to 0$. In this limit, $\overline{S}_{\partial\theta/\partial x_3}$ and $\overline{F}_{\partial\theta/\partial x_3}$ approach,

respectively, the values of 0 and 3 (see figures 4*a*2 and 4*b*2). Hence, the probability density function (p.d.f.) of $\partial\theta/\partial x_3$ becomes approximately Gaussian; this is also the case for the p.d.f.s of $\partial\theta/\partial x_1$ and $\partial\theta/\partial x_2$ (figure not shown). At very low $\overline{Pe}_{\lambda_\theta}$, the anisotropy of scalar fluctuation measured by $\overline{g}_\theta$ and $\overline{F}$ is maximal, which arises solely from the kinematic constraint on the velocity correlation function under the negligible effect of the convective term (see § 3.4). As $\overline{Pe}_{\lambda_\theta}$ increases, the convective term affects the anisotropy in a way that makes the p.d.f. of $\partial\theta/\partial x_3$ positively skewed for moderate $\overline{Pe}_{\lambda_\theta}$ and tends to recover its symmetry for high $\overline{Pe}_{\lambda_\theta}$ (figure 4*a*2). It should be stressed that the second-order moment of fluctuation gives the width of the p.d.f., while the skewness, the third-order moment, measures the asymmetry of the p.d.f. Therefore, the anisotropy of the scalar gradients can exist even when their skewness is zero. Indeed, the fluctuations of the scalar gradients at very low $\overline{Pe}_{\lambda_\theta}$ correspond to the anisotropic state with zero skewness, symmetric (almost Gaussian) p.d.f.s with different widths, while those at large $\overline{Pe}_{\lambda_\theta}$ lead to nearly symmetric (non-Gaussian) p.d.f.s with almost the same widths, suggesting a nearly isotropic state.

Figure 5(*c*) shows the $\overline{Pe}_{\lambda_\theta}$-dependence of $\kappa/\overline{\kappa}_T$. Similarly to $\overline{g}_\theta$ and $\overline{F}$, the plots of $\kappa/\overline{\kappa}_T$ for the four different $\overline{Re}_\lambda$ are found to collapse well onto a single curve. Here, $\kappa/\overline{\kappa}_T$ increases drastically with decreasing $\overline{Pe}_{\lambda_\theta}$. The increasing behaviour follows $\kappa/\overline{\kappa}_T \propto \overline{Pe}_{\lambda_\theta}^{-2}$ in the range of $\overline{Pe}_{\lambda_\theta} \lesssim 1$, where $\overline{F}$ becomes a close to the asymptotic value of -0.2 (figure 5*b*). Note that the power law $\kappa/\overline{\kappa}_T \propto \overline{Pe}_{\lambda_\theta}^{-2}$ can be derived with dimensional analysis (see appendix A). The slope observed above $\overline{Pe}_{\lambda_\theta} \approx 5$ is shallower, which is attributed to the scalar transport by the velocity field. Finally, we note that the plots of the anisotropy parameter $\overline{a}$ for the four different $\overline{Re}_\lambda$ also collapse well onto a single curve (see figure 5*d*). The effect of $\kappa/\overline{\kappa}_T$ in $\overline{a}$ becomes more manifest for decreasing $\overline{Pe}_{\lambda_\theta}$. As $\overline{Pe}_{\lambda_\theta}$ is decreased below $\overline{Pe}_{\lambda_\theta} \approx 5$, $\kappa/\overline{\kappa}_T$ becomes significantly larger than $|\overline{F}|$ (i.e., $\kappa/\overline{\kappa}_T \gg |\overline{F}|$); consequently, $\overline{a}$ approaches unity so that the second-order Legendre contribution is almost as significant as the zero-order one.

Based on figure 5, it is reasonable to consider that the variations of $\overline{g}_\theta$, $\overline{F}$, $\kappa/\overline{\kappa}_T$ and $\overline{a}$ are characterised by universal functions of $\overline{Pe}_{\lambda_\theta}$, and thus we conclude that $\overline{Pe}_{\lambda_\theta}$ is a key parameter to determine the degree of small-scale anisotropy of scalar fluctuations under a uniform mean scalar gradient.

3.4. *Asymptotic behaviour of scalar fluctuations as* $\overline{Pe}_{\lambda_\theta} \to 0$

Having found in figure 5(*a*) that the value of $\overline{g}_\theta$ approaches 0.5 as $\overline{Pe}_{\lambda_\theta} \to 0$, we further investigate the asymptotic behaviour of scalar fluctuations. Figure 6 shows mixed spectral skewness $S_\theta(t)$, computed as

$$S_\theta(t) = \frac{2}{15}\frac{\displaystyle\int_0^\infty k^2 T_\theta(k,t)\,\mathrm{d}k}{(\epsilon(t)/15\nu)^{1/2}(\chi(t)/6\kappa)}, \tag{3.7}$$

where $T_\theta(k,\ t)$ is the scalar-variance transfer function appearing in the spectral equation for the scalar variance (see Watanabe & Gotoh (2004, 2007), for details). Here, $S_\theta(t)$ is a measure of the degree of interaction between velocity and scalar fluctuation fields (Kerr 1985; Briard & Gomez 2016). Irrespective of the value of $\overline{Re}_\lambda$, $-\overline{S}_\theta$ approaches zero with decreasing $\overline{Pe}_{\lambda_\theta}$, where the effect of turbulent scalar mixing becomes insignificant (figure 6).

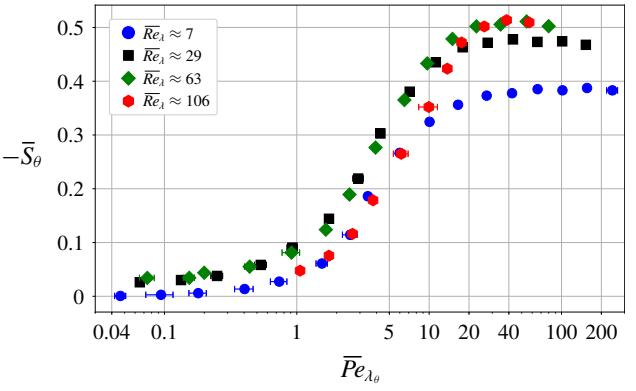

FIGURE 6. Time-averaged mixed spectral skewness $-\overline{S}_\theta$ as a function of $\overline{Pe}_{\lambda_\theta}$. Blue circles, black squares, green diamonds and red hexagons indicate data for $\overline{Re}_\lambda \approx 7$, 29, 63 and 106, respectively. Horizontal error bars denote the temporal standard deviations of $Pe_{\lambda_\theta}(t)$ and vertical error bars denote those of $-S_\theta(t)$.

Based on this behaviour of mixed spectral skewness, we next consider the asymptotic condition in Fourier space in the limit of $\overline{Pe}_{\lambda_\theta} \to 0$,

$$\kappa k^2 \widehat{\theta}(\boldsymbol{k}, t) \approx -\Gamma \widehat{u}_3(\boldsymbol{k}, t), \tag{3.8}$$

where the time-derivative term and convective term are negligibly small. In order to assess its validity, we introduce the residual function, $\widehat{\Delta}(\boldsymbol{k}, t)$, as

$$\widehat{\Delta}(\boldsymbol{k}, t) = \widehat{\theta}(\boldsymbol{k}, t) + \frac{\Gamma}{\kappa k^2} \widehat{u}_3(\boldsymbol{k}, t), \tag{3.9}$$

and consider the asymptotic behaviour of the spectrum $E_\Delta(k, t)$ of this function,

$$E_\Delta(k, t) = \int_0^{2\pi} \mathrm{d}\psi \int_0^{\pi} \mathrm{d}\phi k^2 \sin\phi \widehat{\Delta}(\boldsymbol{k}, t) \widehat{\Delta}(-\boldsymbol{k}, t), \tag{3.10}$$

in comparison with $E_\theta(k, t)$. If $E_\Delta(k, t) \ll E_\theta(k, t)$, then (3.8) holds. Figure 7 shows the variation of the magnitude relationship between $\overline{E}_\Delta(k)$ and $\overline{E}_\theta(k)$ with respect to $\overline{Pe}_{\lambda_\theta}$, for $\overline{Re}_\lambda \approx 69$. At moderate $\overline{Pe}_{\lambda_\theta}$, $\overline{E}_\Delta(k)$ is not negligible (see figures 7*a* and 7*b*) so that (3.8) is not applicable. As $\overline{Pe}_{\lambda_\theta}$ is further decreased, $\overline{E}_\Delta(k)$ tends to become smaller relative to $\overline{E}_\theta(k)$. As for run C4096i (figure 7*d*), in particular, $\overline{E}_\Delta(k)$ is approximately two to three orders of magnitude smaller than $\overline{E}_\theta(k)$ at any wavenumber, meaning that (3.8) is valid. Note that such a tendency with respect to $\overline{Pe}_{\lambda_\theta}$ is found for the other Reynolds numbers. The result above is numerical evidence for justifying that (3.8) is the asymptotic condition in the limit of $\overline{Pe}_{\lambda_\theta} \to 0$.

Using (3.8), in the following, we analytically derive the asymptotic value of $\overline{g}_\theta = 0.5$ as $Pe_{\lambda_\theta} \to 0$, as found in figure 5(*a*). Here, we may compute $\overline{g}_\theta$ as

$$\overline{g}_\theta = \overline{\iiint k_3^2 |\widehat{\theta}|^2(\boldsymbol{k}, t)\, \mathrm{d}\boldsymbol{k}} \Big/ \overline{\iiint k_1^2 |\widehat{\theta}|^2(\boldsymbol{k}, t)\, \mathrm{d}\boldsymbol{k}}. \tag{3.11}$$

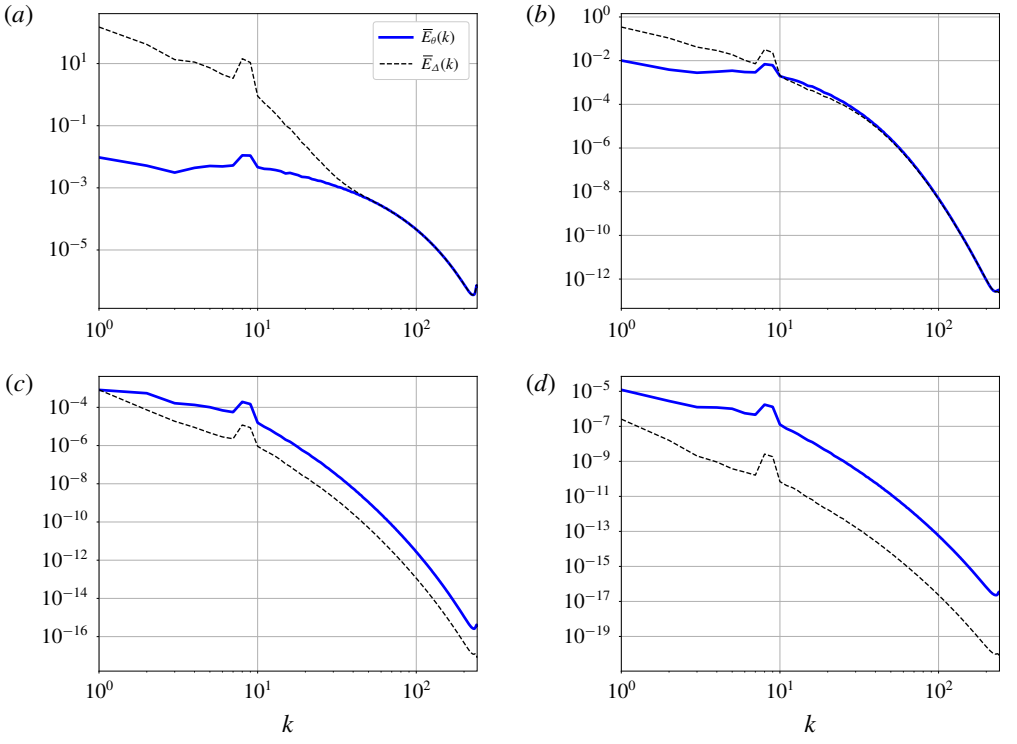

FIGURE 7. Comparisons between $\overline{E}_\theta(k)$ and $\overline{E}_\Delta(k)$ at $\overline{Re}_\lambda \approx 69$ and four different Schmidt numbers. (*a*) Run C1, $Sc = 1$ and $\overline{Pe}_{\lambda_\theta} = 34.6$; (*b*) run C16i, $Sc = 1/16$ and $\overline{Pe}_{\lambda_\theta} = 6.50$; (*c*) run C256i, $Sc = 1/256$ and $\overline{Pe}_{\lambda_\theta} = 0.912$; (*d*) run C4096i, $Sc = 1/4096$ and $\overline{Pe}_{\lambda_\theta} = 0.0742$.

We calculate the numerator in (3.11) using (3.8) as

$$\begin{aligned}\overline{\iiint k_3^2|\widehat{\theta}(\boldsymbol{k},t)|^2\,\mathrm{d}\boldsymbol{k}} &\approx \frac{\Gamma^2}{\kappa^2}\iiint \frac{k_3^2}{k^4}\overline{|\widehat{u}_3|^2}(\boldsymbol{k})\,\mathrm{d}\boldsymbol{k}\\ &= \frac{\Gamma^2}{\kappa^2}\iiint \frac{k_3^2}{k^4}P_{33}(\boldsymbol{k})\overline{Q_u^*}(k)\,\mathrm{d}\boldsymbol{k}\\ &= \frac{8\pi}{15}\frac{\Gamma^2}{\kappa^2}\int \overline{Q_u^*}(k)\,\mathrm{d}k, \end{aligned} \tag{3.12}$$

where $Q_u^*(k,t) = E_u(k,t)/(4\pi k^2)$ is the orientation-averaged energy spectral density. Similarly to (3.12), we obtain the value of the denominator in (3.11) as $\overline{\iiint k_1^2|\widehat{\theta}(\boldsymbol{k},t)|^2\,\mathrm{d}\boldsymbol{k}} \approx (16\pi/15)(\Gamma^2/\kappa^2)\int \overline{Q_u^*}(k)\,\mathrm{d}k$. Thus, we find that $\overline{g}_\theta \approx (8\pi/15)(\Gamma^2/\kappa^2)\int \overline{Q_u^*}(k)\,\mathrm{d}k/(16\pi/15)(\Gamma^2/\kappa^2)\int \overline{Q_u^*}(k)\,\mathrm{d}k = 0.5$.

4. Summary and discussion

In the present paper, we have shown that the degree of small-scale anisotropy of scalar fluctuations, which are convected by homogeneous isotropic turbulence under a uniform mean scalar gradient, can be well characterised by $\overline{Pe}_{\lambda_\theta}$ (figure 5).

We have also demonstrated that large-scale anisotropic scalar structures, which elongate along the direction of the mean scalar gradient, emerge irrespective of $\overline{Re}_\lambda$, as long as $\overline{Pe}_{\lambda_\theta}$ is sufficiently low (figure 2*c*). Despite the anisotropy, the isotropic part of the scalar variance spectrum has a power-law scaling slightly shallower than $k^{-17/3}$. The convection of small-scale scalar fluctuations by the isotropic flow becomes significantly weaker with decreasing $\overline{Pe}_{\lambda_\theta}$ below $\overline{Pe}_{\lambda_\theta} \approx 20$, as observed in the behaviour of mixed spectral skewness (figure 6).

We emphasise that the systematic dependence of anisotropic scalar fluctuation on a control parameter is found when arranging data in terms of $\overline{Pe}_{\lambda_\theta}$, and not Sc, as shown in figure 5(*d*). Note that the plots of our data are not better collapsed when using $Pe_\lambda = ScRe_\lambda$ rather than Pe_{λ_θ}, suggesting that the use of λ_θ is essential. Here, we consider the ratio R of the net convective scalar transport rate to the net diffusive scalar transport rate, which is formulated based on (2.3) as

$$R = \frac{(\text{net convective scalar transport rate})}{(\text{net diffusive scalar transport rate})} \sim \frac{u_i \nabla\theta}{\kappa \nabla^2\theta}. \tag{4.1}$$

It should be noted that the gradient and Laplacian operate on the scalar fluctuation field, not on the velocity field. Since the Batchelor scale does not include any information about scalar fluctuations, it is reasonable to adopt the scalar Taylor microscale for characterising the spatial derivatives of scalar field. On the basis of the derivation of the scalar Taylor microscale, we make the following replacements in (4.1) as

$$u_i \to u', \quad \nabla\theta \to \frac{\theta'}{\lambda_\theta}, \quad \nabla^2\theta \to \frac{\theta'}{\lambda_\theta^2}, \tag{4.2a–c}$$

thereby yielding

$$R \sim \frac{u'\theta'/\lambda_\theta}{\kappa\theta'/\lambda_\theta^2} = \frac{u'\lambda_\theta}{\kappa} = Pe_{\lambda_\theta}. \tag{4.3}$$

We thus find that, by means of dimensional analysis, the ratio R is transformed into the Péclet number based on λ_θ; λ_u is irrelevant herein.

In order to obtain a further insight into the role of Pe_{λ_θ}, we express it in terms of two different time scales as

$$Pe_{\lambda_\theta} = \frac{\lambda_\theta^2/\kappa}{\lambda_\theta/u'} = \frac{\tau_\theta}{\tau_{u\theta}}, \tag{4.4}$$

where $\tau_\theta = \lambda_\theta^2/\kappa$ and $\tau_{u\theta} = \lambda_\theta/u'$ are the time scales of scalar diffusion and scalar convection, respectively, based on λ_θ. When $Pe_{\lambda_\theta} \gg 1$ (i.e., $\tau_{u\theta} \ll \tau_\theta$), small-scale scalar fluctuations are effectively convected and smeared out by the velocity field before diffusing. When $Pe_{\lambda_\theta} \ll 1$ (i.e., $\tau_{u\theta} \gg \tau_\theta$), on the other hand, the scalar diffusion process proceeds much more quickly than the scalar transport process. Because of the action of the rapid scalar diffusion and the uniform mean scalar gradient, large-scale anisotropic scalar structures emerge opposing the isotropisation due to the transport by isotropic velocity field. Note that such large-scale anisotropic scalar structures do not appear when a white Gaussian scalar source is applied as opposed to a uniform mean scalar gradient. The macroscopic scalar gradient serves as a source of scalar fluctuations that are convected and diffused to merge into large-scale anisotropic scalar structures (figure 2*c*).

In the present paper, we have investigated anisotropic scalar fluctuation based on one-point statistics. Having a clear map of variation of small-scale anisotropy of scalar fluctuations with respect to $\overline{Pe}_{\lambda_\theta}$ (figure 5*d*), our analysis will be extended to scale-by-scale anisotropy of scalar fluctuations using a Legendre polynomial expansion, which provides the angle dependence of scalar fluctuation at various scales (Gotoh *et al.* 2011; Hill 2017). We believe that this approach would provide a further insight into anisotropic scalar fluctuations.

Acknowledgements

T.Y. and T.G. express their thanks for discussions with, and comments from, Dr Hill. The authors are grateful to the anonymous reviewers for their insightful comments. The computational supports were provided by NIFS (grant nos NIFS18KNSS105 and NIFS20KNSS143), JHPCN (jh200006), HPCI (hp200072) and JAMSTEC. This work was supported by MEXT KAKENHI (grant nos 15H02218, 20H00225 and 20H02066) and JSPS KAKENHI (grant nos 18K03925 and 18K13611).

Declaration of interests

The authors report no conflict of interest.

Appendix A. Derivation of $\kappa/\overline{\kappa}_T \propto \overline{Pe}_{\lambda_\theta}^{-2}$ in the low Péclet number range

Using dimensional analysis, we derive the power law $\kappa/\overline{\kappa}_T \propto \overline{Pe}_{\lambda_\theta}^{-2}$, which is found in the low $\overline{Pe}_{\lambda_\theta}$ range in figure 5(*c*). We start with the time-averaged balance between the scalar dissipation rate and the input rate of scalar variance,

$$\overline{\chi} = -2\Gamma\overline{\langle u_3\theta\rangle}. \tag{A 1}$$

Averaging (3.6) over time and then substituting (A 1) into it, we have

$$\frac{\kappa}{\overline{\kappa}_T} = \frac{2\kappa\Gamma^2}{\overline{\chi}} = \frac{2\kappa\Gamma^2}{-2\Gamma\overline{\langle u_3\theta\rangle}} \sim \frac{\kappa\Gamma}{u'\theta'}. \tag{A 2}$$

When $\overline{Pe}_{\lambda_\theta}$ is sufficiently low, as discussed in § 3.4, the asymptotic condition (3.8) holds. This condition, defined in Fourier space, is equivalent to

$$\kappa\nabla^2\theta(\boldsymbol{x}, t) \approx \Gamma u_3(\boldsymbol{x}, t) \tag{A 3}$$

in physical space. Manipulating (A 3) using (4.2), we find that

$$\theta' \sim \frac{\Gamma u'\lambda_\theta^2}{\kappa}. \tag{A 4}$$

Then we substitute (A 4) into (A 2), which yields that

$$\frac{\kappa}{\overline{\kappa}_T} \sim \frac{\kappa\Gamma}{u'\theta'} \sim \frac{\kappa\Gamma}{u'}\frac{\kappa}{\Gamma u'\lambda_\theta^2} = \left(\frac{\kappa}{u'\lambda_\theta}\right)^2 = Pe_{\lambda_\theta}^{-2}. \tag{A 5}$$

It thus follows that

$$\frac{\kappa}{\overline{\kappa}_T} \propto \overline{Pe}_{\lambda_\theta}^{-2}. \tag{A 6}$$

REFERENCES

BATCHELOR, G. K. 1959 Small-scale variation of convected quantities like temperature in turbulent fluid. Part 1. General discussion and the case of small conductivity. *J. Fluid Mech.* **5**, 113–133.

BATCHELOR, G. K., HOWELLS, I. D. & TOWNSEND, A. A. 1959 Small-scale variation of convected quantities like temperature in turbulent fluid. Part 2. The case of large conductivity. *J. Fluid Mech.* **5**, 134–139.

BRIARD, A. & GOMEZ, T. 2016 Mixed-derivative skewness for high Prandtl and Reynolds numbers in homogeneous isotropic turbulence. *Phys. Fluids* **28**, 081703.

BUDWIG, R., TAVOULARIS, S. & CORRSIN, S. 1985 Temperature fluctuations and heat flux in grid-generated isotropic turbulence with streamwise and transverse mean-temperature gradients. *J. Fluid Mech.* **153**, 441–460.

CORRSIN, S. 1951 On the spectrum of isotropic temperature fluctuations in an isotropic turbulence. *J. Appl. Phys.* **22**, 469–473.

DONZIS, D. A. & YEUNG, P. K. 2010 Resolution effects and scaling in numerical simulations of passive scalar mixing in turbulence. *Physica* D **239**, 1278–1287.

ECKERT, E. R. G. & DRAKE, R. M. 1959 *Heat and Mass Transfer*, 2nd edn. McGraw-Hill Education.

GOTOH, T., HATANAKA, S. & MIURA, H. 2012 Spectral compact difference hybrid computation of passive scalar in isotropic turbulence. *J. Compt. Phys.* **231**, 7398–7414.

GOTOH, T. & WATANABE, T. 2015 Power and nonpower laws of passive scalar moments convected by isotropic turbulence. *Phys. Rev. Lett.* **115**, 114502.

GOTOH, T., WATANABE, T. & MIURA, H. 2014 Spectrum of passive scalar at very high Schmidt number in turbulence. *Plasma Fusion Res.* **9**, 3401019.

GOTOH, T., WATANABE, T. & SUZUKI, Y. 2011 Universality and anisotropy in passive scalar fluctuations in turbulence with uniform mean gradient. *J. Turbul.* **12**, 1–27.

GOTOH, T. & YEUNG, P. K. 2012 Passive scalar transport in turbulence: a computational perspective. In *Ten Chapters in Turbulence* (ed. P. A. Davidson, Y. Kaneda & K. R. Sreenivasan), pp. 87–131. Cambridge University Press.

HILL, R. J. 2017 Spectra of turbulently advected scalars that have small Schmidt number. *Phys. Rev. Fluids* **2**, 094601.

HOLZER, M. & SIGGIA, E. D. 1994 Turbulent mixing of a passive scalar. *Phys. Fluids* **6**, 1820–1837.

KERR, R. M. 1985 Higher-order derivative correlations and the alignment of small-scale structures in isotropic numerical turbulence. *J. Fluid Mech.* **153**, 31–58.

LEPORE, J. & MYDLARSKI, L. 2012 Finite-Péclet-number effects on the scaling exponents of high-order passive scalar structure functions. *J. Fluid Mech.* **713**, 453–481.

MYDLARSKI, L. & WARHAFT, Z. 1998 Passive scalar statistics in high-Péclet-number grid turbulence. *J. Fluid Mech.* **358**, 135–175.

OBUKHOV, A. M. 1949 Structure of the temperature field in turbulent flow. *Izv. Akad. Nauk SSSR* **13**, 58–69.

O'GORMAN, P. A. & PULLIN, D. I. 2005 Effect of Schmidt number on the velocity-scalar cospectrum in isotropic turbulence with a mean scalar gradient. *J. Fluid Mech.* **532**, 111–140.

SCHUMACHER, J., SREENIVASAN, K. R. & YEUNG, P. K. 2003 Schmidt number dependence of derivative moments for quasi-static straining motion. *J. Fluid Mech.* **479**, 221–230.

SCHUMACHER, J., SREENIVASAN, K. R. & YEUNG, P. K. 2005 Very fine structures in scalar mixing. *J. Fluid Mech.* **531**, 113–122.

SREENIVASAN, K. R. 1991 On local isotropy of passive scalars in turbulent shear flows. *Proc. R. Soc. Lond.* A **434**, 165–182.

SREENIVASAN, K. R. 1996 The passive scalar spectrum and the Obukhov–Corrsin constant. *Phys. Fluids* **8**, 189–196.

SREENIVASAN, K. R. 2018 Turbulent mixing: a perspective. *Proc. Natl Acad. Sci. USA* **116**, 18175–18183.

SREENIVASAN, K. R. & TAVOULARIS, S. 1980 On the skewness of the temperature derivative in turbulent flows. *J. Fluid Mech.* **101**, 783–795.

TONG, C. & WARHAFT, Z. 1994 On passive scalar derivative statistics in grid turbulence. *Phys. Fluids* **6**, 2165–2176.

WARHAFT, Z. 2000 Passive scalars in turbulent flows. *Annu. Rev. Fluid Mech.* **32**, 203–240.

WATANABE, T. & GOTOH, T. 2004 Statistics of a passive scalar in homogeneous turbulence. *New J. Phys.* **6**, 40.

WATANABE, T. & GOTOH, T. 2007 Inertial-range intermittency and accuracy of direct numerical simulation for turbulence and passive scalar turbulence. *J. Fluid Mech.* **590**, 117–146.

YEUNG, P. K., DONZIS, D. A. & SREENIVASAN, K. R. 2005 High-Reynolds-number simulation of turbulent mixing. *Phys. Fluids* **17**, 081703.

YEUNG, P. K. & SREENIVASAN, K. R. 2013 Spectrum of passive scalars of high molecular diffusivity in turbulent mixing. *J. Fluid Mech.* **716**, R14.

YEUNG, P. K. & SREENIVASAN, K. R. 2014 Direct numerical simulation of turbulent mixing at very low Schmidt number with a uniform mean gradient. *Phys. Fluids* **26**, 015107.

YEUNG, P. K., XU, S., DONZIS, D. A. & SREENIVASAN, K. R. 2004 Simulations of three-dimensional turbulent mixing for Schmidt numbers of the order 1000. *Flow Turbul. Combust.* **72**, 333–347.

YEUNG, P. K., XU, S. & SREENIVASAN, K. R. 2002 Schmidt number effects on turbulent transport with uniform mean scalar gradient. *Phys. Fluids* **14**, 4178–4191.